

Internal tides, nonlinear internal wave trains, and mixing in the Faroe-Shetland Channel

R. A. Hall,^{1,2,3} J. M. Huthnance,¹ and R. G. Williams²

Received 17 February 2010; revised 29 October 2010; accepted 9 December 2010; published 5 March 2011.

[1] A semidiurnal internal tide and trains of near-bed nonlinear internal waves were observed on the southeastern bank of the Faroe-Shetland Channel. The depth-integrated M_2 internal tide energy flux was 140 W m^{-1} up-slope and 154 W m^{-1} along-slope to the southwest. The majority of the energy flux was contained within the main pycnocline, where the slope was supercritical. A numerical model of the M_2 tide successfully reproduces the observed maxima in the pycnocline but overestimates depth-integrated baroclinic energy fluxes by 15%–45%. The model results suggest that the internal tide in the channel is generated at multiple sites, including the northwestern bank and the Wyville Thomson Ridge. On the northern flank of the ridge, modeled energy fluxes are over an order of magnitude larger than in the channel, $>5 \text{ kW m}^{-1}$. The turbulent kinetic energy dissipation rate inferred from the observed internal tide energy flux, by assuming that all the energy in the pycnocline was dissipated on the slope, was $1.3 \times 10^{-7} \text{ W kg}^{-1}$, a factor of 4 larger than that inferred from Thorpe scale analysis ($3 \times 10^{-8} \text{ W kg}^{-1}$). This suggests that the high level of mixing on the slope can be accounted for by the internal tide, even if the majority of the energy was reflected. The nonlinear internal wave energy flux was up-slope and intermittent; peak energy fluxes reached 200 W m^{-1} but were typically of order 10 W m^{-1} . The wave trains were likely tidally forced and may have been a nonlinear manifestation of the internal tide.

Citation: Hall, R. A., J. M. Huthnance, and R. G. Williams (2011), Internal tides, nonlinear internal wave trains, and mixing in the Faroe-Shetland Channel, *J. Geophys. Res.*, 116, C03008, doi:10.1029/2010JC006213.

1. Introduction

[2] Internal tides and internal waves are an important mechanism for the transfer of energy in the ocean and may sustain high levels of mixing on continental shelf slopes [Nash *et al.*, 2004, 2007] and at shelf breaks [Pingree *et al.*, 1986; New and Pingree, 1990]. Enhanced mixing from internal wave breaking on the shelf slopes that bound the Faroe-Shetland Channel (FSC) is of potential importance given the channels role in the exchange of water masses between the Nordic Seas and the North Atlantic [Mauritzen *et al.*, 2005; Hosegood *et al.*, 2005].

[3] The FSC is located north of Scotland and separates the Shetland and Faroe shelves. To the northeast, the channel is open to the Norwegian Sea, while the southwestern end is partially closed by the Wyville Thomson Ridge and connected to the Iceland Basin by the Faroe Bank Channel (Figure 1a). The FSC and Faroe Bank Channel together form one of two

main passageways through which deep water formed in the Nordic Seas overflows the Greenland-Scotland Ridge into the North Atlantic [Dickson and Brown, 1994; Hansen and Østerhus, 2000], the other being the Denmark Strait.

[4] In the FSC near the surface, North Atlantic Water flows northeast, along the edge of the Shetland shelf, into the Norwegian Sea [Turrell *et al.*, 1999]. Below the main pycnocline, Norwegian Sea Deep Water flows southwest, along the axis of the channel, then through the Faroe Bank Channel into the Iceland Basin [Saunders, 1990; Borenäs and Lundberg, 2004]. As the deep water overflows the Faroe Bank Channel sill, it mixes with overlying water masses to form North Atlantic Deep Water. Intermittently, Norwegian Sea Deep Water overflows the Wyville Thomson Ridge into the Rockall Trough [Sherwin *et al.*, 2008].

[5] Turbulent mixing in the FSC may modify the θ - S properties of the exchanging water masses, potentially affecting large-scale ocean circulation through the composition of North Atlantic Deep Water. Below from the surface mixed layer, mixing in the channel is likely to be dominated internal wave interactions, specifically those of tidal frequencies (internal tides). Mixing may be enhanced on the shelf slopes that bound the channel by critical reflection of internal waves from the sloping topography.

[6] When internal waves approach a slope from deep water, the onshore/offshore direction of propagation after reflection

¹National Oceanography Centre, Liverpool, UK.

²Department of Earth and Ocean Sciences, University of Liverpool, Liverpool, UK.

³Now at Department of Oceanography, University of Hawai'i at Mānoa, Honolulu, Hawaii, USA.

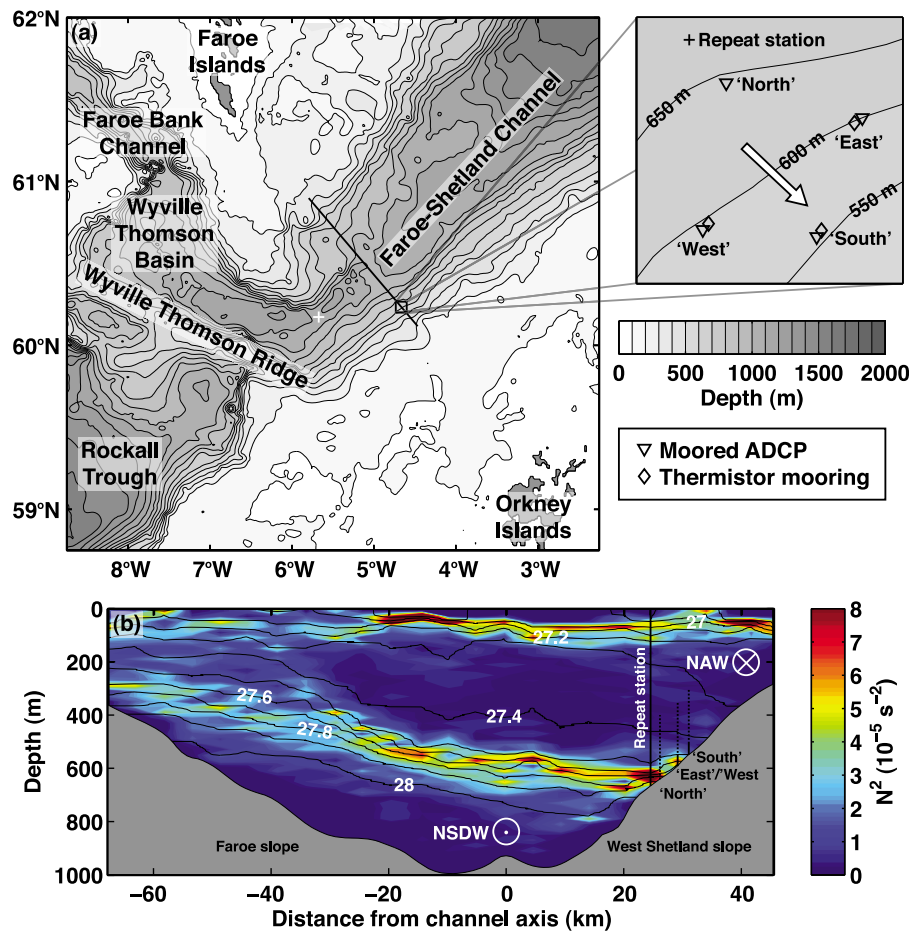


Figure 1. (a) Bathymetry of the Faroe-Shetland Channel and the locations of the across-channel section (black line), mooring array (black square), and CTD casts used for the model stratification (white cross). The contour interval is 100 m. Enlargement shows the locations of the individual moorings in the array and the repeat station. The arrow is the direction of nonlinear internal wave propagation. (b) N^2 and contours of σ_θ along the across-channel section shown in Figure 1a, with the locations of the moorings and repeat station. Also shown is the direction of NAW/NSDW exchange flow.

is determined by the ratio of the topographic slope to the internal wave characteristic slope,

$$\alpha = \frac{s_{\text{topog}}}{s_{\text{wave}}} = \frac{\partial H / \partial x}{[(\omega^2 - f^2) / (N^2 - \omega^2)]^{1/2}}, \quad (1)$$

where H is the total depth, x is across-slope distance, ω is the angular frequency of the wave, f is the inertial frequency, and N is the buoyancy frequency. If $\alpha < 1$ (subcritical) the waves will continue to shoal after reflection. If $\alpha > 1$ (supercritical) reflected waves will propagate back into deeper water. For downward propagating internal wave characteristics approaching a slope from offshore, energy density increases upon reflection because the separation between adjacent characteristics narrows, concentrating the energy into a smaller area. If $\alpha = 1$ (critical) linear theory breaks down and energy is trapped at the boundary, leading to nonlinear effects and potentially wave breaking.

[7] Along the southeastern bank of the FSC, the main pycnocline meets the West Shetland slope and permanent stratification is maintained close to the seabed. Near-bottom buoyancy frequency is high enough ($N^2 > 10^{-5} \text{ s}^{-2}$) for supercritical reflection of semidiurnal internal tides to occur,

despite the topographic slope being gentle (0.02). Above and below the pycnocline, the slope is subcritical to semidiurnal internal tides. Mixing is likely enhanced in the bands of near-critical slope between the subcritical and supercritical areas. As the vertical separation between adjacent internal wave characteristics decreases with increasing buoyancy frequency, internal wave energy may become concentrated in the pycnocline and potentially be an important source of energy for mixing where the pycnocline meets the slope.

[8] *Sherwin* [1991] observed a 37 m amplitude M_2 internal tide in the main pycnocline at the southwestern end of the FSC, near the Wyville Thomson Ridge, and estimated the energy flux to be 4.7 kW m^{-1} . Assuming the internal tide was generated at the ridge, and using the analytical model of *Baines* [1982], *Sherwin* [1991] predicted the energy flux on the northern flank to be $1.4\text{--}3.2 \text{ kW m}^{-1}$. It was speculated that the internal tide propagates along the channel, becoming nonlinear at the boundaries, and that the energy is either dissipated by mixing on the shelf slopes, or leaks upward onto the Shetland and Faroe shelves. More recently, *Gerkema* [2002] used a numerical internal tide generation model to simulate the baroclinic spring-neap cycle in the FSC and

identified a phase shift with respect to the barotropic spring-neap cycle. *Hosegood and van Haren* [2004] observed trains of nonlinear internal waves propagating up the West Shetland slope near the seabed. These wave trains occurred aperiodically, suggesting that they were not directly tidally forced, but were associated with high (order 10^{-7} W kg $^{-1}$) turbulent kinetic energy dissipation rates. The generation of nonlinear dispersive internal tides and their disintegration into wave trains has been simulated by *Gerkema and Zimmerman* [1995] and *Gerkema* [1996] using a two-layer model. However, it is unclear how far internal tides generated at the Wyville Thomson Ridge propagate along the FSC, their relation to the observed nonlinear wave trains, and whether they enhance mixing at the boundaries.

[9] In September 2005, a slope mixing experiment was undertaken on the West Shetland slope to make measurements of internal waves and their induced mixing. In this study, observations of internal waves from the experiment are combined with a numerical model of the M_2 tide in the FSC region to investigate (1) the generation of internal tides at the Wyville Thomson Ridge and in the channel, (2) internal tide and nonlinear internal wave energy fluxes on the West Shetland slope, and (3) dissipation of these internal waves as a source of energy for mixing. The instrumentation, background hydrography, and internal wave observations from the slope mixing experiment are described in sections 2 and 3. The numerical model setup and validation is described in section 4. Internal tide energy fluxes from the observations and the model output are calculated in section 5. The energy flux associated with trains of nonlinear internal waves observed on the slope is estimated in section 6. Dissipation of the internal waves and the resulting mixing is considered in section 7. Other sources of energy available for mixing and the global context are discussed in section 8.

2. Slope Mixing Experiment

2.1. Instrumentation

[10] The research vessel FS *Poseidon* was used to deploy an array of ADCPs and thermistor moorings on the West Shetland slope between 7 and 21 September 2005 (Figure 1a). Four upward looking ADCPs were arranged in a square ~ 5 km across, about the 600 m isobath, to sample through the main pycnocline close to where it met the slope (Figure 1b). At the “South” and “West” corners of the square, 150 kHz ADCPs with 200 m range were deployed, sampling in 4 m vertical bins; a 75 kHz ADCP with 250 m range was deployed in the “North” corner (8 m bins); a 600 kHz ADCP with shorter 40 m range was deployed in the “East” corner (2 m bins). Three 50 m thermistor moorings were deployed next to the ADCP moorings at the “East,” “South,” and “West” corners of the square. The thermistors were 4 m apart along the mooring cable. On the “East” and “West” moorings a CTD logger was attached 4 m above the seabed. All the ADCPs and most of the thermistors had 2 min sampling (some thermistors were set to sample every 4 min due to memory constraints); the CTD loggers sampled every minute. This arrangement of instruments, in a three-dimensional mooring array rather than a single line of moorings, allowed both the speed and direction of internal waves to be resolved, provided individual waves were observed in three or more of the mooring time series.

[11] A repeat station over the 680 m isobath, adjacent to the moorings, was occupied for 24 h during the deployments (11–12 September 2005) and a full-depth CTD cast recorded every hour. A full-depth CTD section across the FSC was also carried out to ascertain the background hydrography. The resolution of the CTD was 1 dbar after processing, but the original 24 Hz sampling frequency was retained for Thorpe scale analysis (~ 0.04 m resolution). A 300 kHz lowered ADCP, sampling in 4 m vertical bins, was also attached to the rosette.

2.2. Background Hydrography

[12] There is a seasonal thermocline over the West Shetland slope in the upper 200 m during the summer months. The main pycnocline intersects the slope with permanent stratification between approximately 550 m and 650 m (e.g., Figure 1b). The pycnocline typically deepens toward the slope and separates warm, saline North Atlantic Water (NAW), flowing northeast along the shelf edge, from the return flow of cold, fresher Norwegian Sea Deep Water (NSDW) along the axis of the channel.

[13] The vertical distance between isopycnals decreases toward the slope, forming a wedge-shaped density field. This “isopycnal pinching” signifies an intermediate water mass is present and is also observed on the Faroe Bank side of the Faroe Bank Channel [*Borenäs et al.*, 2001]. Over the Faroe slope, the northwestern bank of the FSC, stratification is weaker, with isopycnals evenly distributed through the water column.

3. Internal Wave Observations

[14] At the location of the repeat station, the main pycnocline was observed at approximately 600 m, less than 100 m above the seabed (Figure 2). Vertical displacement of the pycnocline suggested an order 10 m amplitude semidiurnal internal tide. Horizontal current velocities were strongly semidiurnal in the lower layer below the pycnocline, with velocity amplitudes of order 0.1 m s $^{-1}$. M_2 harmonic fits to the depth-averaged flow showed barotropic tidal amplitudes were 0.05 m s $^{-1}$ and 0.08 m s $^{-1}$ across and along the slope, respectively.

[15] Higher-frequency, nonlinear internal waves were observed intermittently in the mooring time series (Figure 3). As the pycnocline was maintained close to the seabed, most of the internal waves were bottom-trapped waves of elevation, as observed by *Holloway* [1987] on the Australian North West Shelf and by *Klymak and Moum* [2003] on the Oregon continental shelf. For a two-layer model, there are two solutions to the Korteweg–de Vries (KdV) equation where nonlinearity and nonhydrostatic dispersion balance to permit waves of permanent form; that is, the shape does not change during propagation. These solutions are solitary waves and periodic cnoidal waves, the former has been successfully used for analysis of internal solitary waves in the ocean [e.g., *Apel et al.*, 1985; *Ostrovsky and Stepanyants*, 1989]. On the West Shetland slope, some of the observed waves occurred as individual solitary waves, while others occurred in packets or trains. On a few occasions, the isopycnals did not return to their original rest state after the solitary wave or wave train had passed (Figure 3a), suggesting solibore behavior [*Henye and Hoering*, 1997].

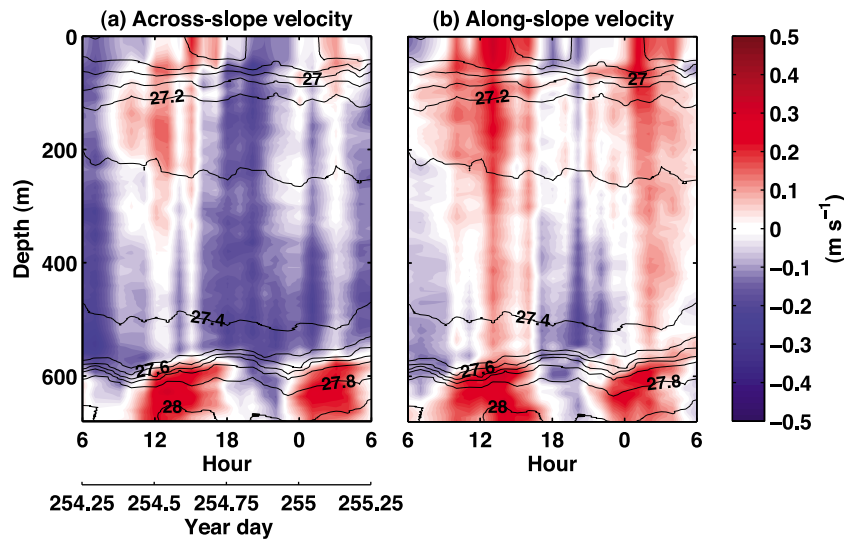


Figure 2. The 24 h time series of (a) across-slope and (b) along-slope velocity from the lowered ADCP at the repeat station. Positive across-slope values are toward the southeast, and positive along-slope values are northeast. Contours of σ_θ from the CTD are also shown.

[16] Each wave train began with a large amplitude (up to 50 m) wave of elevation; subsequent waves generally decreased in amplitude and had periods between 15 and 30 min. This amplitude variation was expected because, for a very shallow lower layer, large amplitude nonlinear waves

travel faster than smaller amplitude waves, evolving into rank-ordered packets over time [Sandstrom and Oakey, 1995]. During some periods of the mooring time series, the wave trains occurred at roughly semidiurnal intervals, unlike those observed by Hosegood and van Haren [2004],

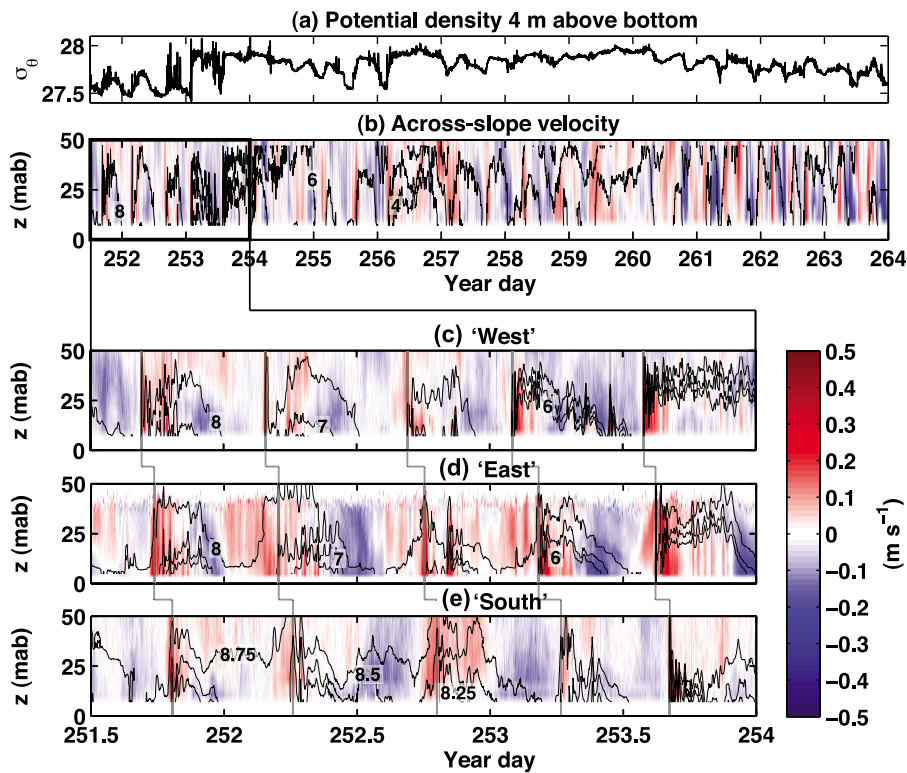


Figure 3. (a) Potential density 4 m above the seabed from the CTD logger on the “West” thermistor mooring. (b) Across-slope velocity and contours of temperature ($^{\circ}\text{C}$) from the “West” thermistor/ADCP mooring pair. Positive velocity values are toward the southeast. Close-ups of across-slope velocity and contours of temperature from the (c) “West,” (d) “East,” and (e) “South” mooring pairs. The gray lines show the leading wave of each wave train in all three mooring time series.

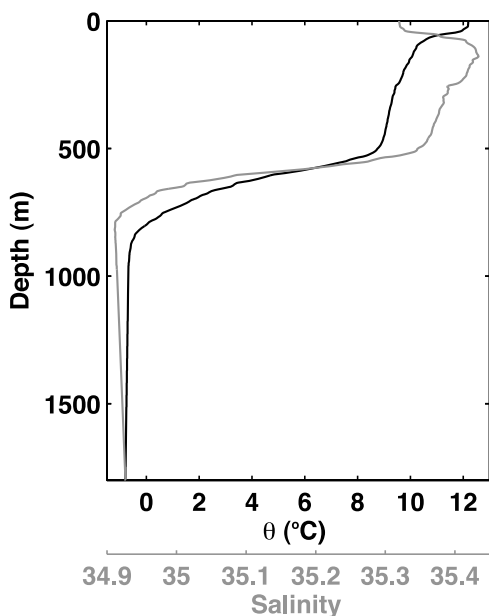


Figure 4. Initial potential temperature (black line) and salinity (gray line) profiles for the model, the average of three CTD casts at $5^{\circ}40'W$, $60^{\circ}10'N$.

so were likely tidally forced. However, the rank ordering suggests that they were observed some distance from their generation site [Carter *et al.*, 2005].

[17] The velocity of the nonlinear waves was measured by tracking the leading wave in each train between the three thermistor/ADCP mooring pairs (Figures 3c–3e). The mean velocity of the leading waves (c) was 0.27 m s^{-1} at an angle of 132° clockwise from north, up the slope and within 10° of perpendicular to the isobaths (indicated by the arrow in Figure 1a). This wave velocity and the observed period implies wavelengths were between 250 and 500 m. The Froude number of the internal waves, $Fr = u/c$, where u is the tidal flow, was up to 2. Wave amplitudes were of the same order as the depth of the lower layer, and amplitude-to-wavelength ratios up to 0.2, reinforcing the nonlinear nature of the waves.

4. Numerical Model

4.1. Model Setup

[18] A modified version of the Princeton Ocean Model (POM) [Blumberg and Mellor, 1987] is used to simulate the M_2 tide in the FSC region. POM is a three-dimensional, nonlinear, hydrostatic, free surface, finite difference, terrain-following (σ coordinate), primitive equation model. The Mellor and Yamada [1982] second-moment turbulence closure scheme is used to calculate diffusivities and viscosities in the vertical and the Smagorinsky [1963] scheme used in the horizontal. The Flather condition [Flather, 1976] is applied at the boundaries so that barotropic energy is transmitted out of the domain. Baroclinic energy is absorbed at the boundaries using the relaxation scheme described by Carter and Merrifield [2007]. The model has previously been used to simulate barotropic and baroclinic tides over the Hawaiian Ridge [Carter *et al.*, 2008; Rainville *et al.*, 2010], the Mid-Atlantic Ridge [Zilberman *et al.*, 2009]

and in Monterey Submarine Canyon [Carter, 2010; Hall and Carter, 2011].

[19] The model domain extends from $13^{\circ}22'W$ to $1^{\circ}58'W$, $58^{\circ}18'N$ to $63^{\circ}54'N$ and is rotated 45° so that the southeastern boundary is parallel to the West Shetland slope. The bathymetry has 1 km horizontal resolution, derived from 1 min Smith and Sandwell [1997] data, and is lightly smoothed with a three-point square running mean. Sixty-one evenly spaced sigma levels are used, giving a vertical resolution between 0.8 and 30 m. Initial conditions are no flow and horizontally uniform stratification; the initial temperature and salinity profiles are the average of three CTD casts at $5^{\circ}40'W$, $60^{\circ}10'N$, approximately halfway between the Wyville Thomson Ridge and the site of the slope mixing experiment, taken on 10 September 2005 (Figure 4). Linear extrapolation is used to extend these observations to the maximum depth within the domain (1800 m). Diffusivities are not applied to the temperature and salinity fields so the stratification is not eroded by mixing. The model is forced at the boundaries with M_2 barotropic velocities. Elevations and normal velocities used to calculate the Flather boundary condition are taken from the TPXO7.2 inverse model [Egbert, 1997; Egbert and Erofeeva, 2002].

[20] The simulation is run for 20 M_2 tidal cycles (10.35 days), a M_2 harmonic analysis is performed over the last six tidal cycles. Harmonic analysis effectively removes any erroneous low-frequency velocities from the calculation of horizontal pressure gradients over steep topography [e.g., Haney, 1991; Mellor *et al.*, 1994].

4.2. Model Validation

[21] Baroclinic velocity from the M_2 harmonic analysis output is validated against M_2 harmonic fits to the across-slope and along-slope baroclinic velocity observations at the repeat station (Figure 5). The velocity maxima in the lower layer below the main pycnocline are well represented, as is the phase lag between the across-slope and along-slope directions. The largest deviation from the observations occurs in the seasonal thermocline, where the vertical phase shift is of the wrong sign.

[22] The model skill is quantitatively assessed by combining the amplitudes and phases of the observed and modeled velocities into a single RMS error estimate in each direction and on each sigma level [Cummins and Oey, 1997; Carter *et al.*, 2008],

$$E_{\text{rms}} = \sqrt{\frac{1}{2}(A_o^2 + A_m^2) - A_o A_m \cos(\phi_o - \phi_m)}, \quad (2)$$

where the subscripts o and m denote the observed and modeled amplitudes (A) and phases (ϕ) of velocity. The depth-averaged RMS error is 0.03 m s^{-1} across-slope (79% of the observed M_2 baroclinic tidal amplitude) and 0.03 m s^{-1} along-slope (86%). Differences between the model output and baroclinic velocity observations may in part be due to differences in stratification. The buoyancy frequency profile at the repeat station (Figure 7a) features a thinner pycnocline than the horizontally uniform model stratification, but higher maximum N^2 values by a factor of 2.

[23] The cotidal plot of modeled M_2 surface elevation amplitudes and phase (Figure 6) shows the amphidromic point east of the Faroe Islands is well resolved. The surface elevation field is in good agreement with previous tidal

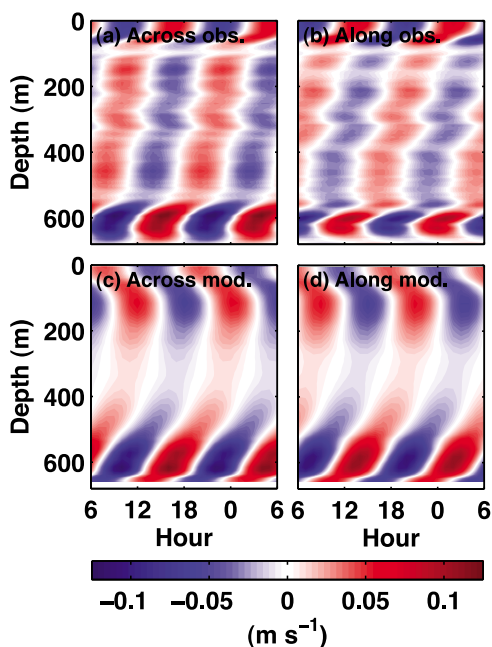


Figure 5. Comparison of model baroclinic velocity with M_2 harmonic fits to the across-slope and along-slope baroclinic velocity observations at the repeat station. Positive across-slope values are toward the southeast, and positive along-slope values are northeast.

modeling efforts in the region [e.g., *Davies et al.*, 2001; *Kwong and Davies*, 2001].

5. Internal Tide Energy Fluxes

[24] The internal (baroclinic) tide energy flux is calculated as $\mathbf{F} = \langle \mathbf{u}'p' \rangle$, where \mathbf{u}' is the velocity perturbation (u' , v' , w'), p' is the pressure perturbation, and $\langle \cdot \rangle$ denotes an average over a tidal cycle [e.g., *Kunze et al.*, 2002; *Nash et al.*, 2005]. The energy flux is calculated from the full-depth lowered ADCP/CTD profiles at the repeat station and from the model harmonic analysis output at all grid points in the domain.

5.1. Observed Energy Flux

[25] For the observed energy flux, semidiurnal velocity perturbations and density anomalies (ρ') are found from M_2 harmonic fits to horizontal velocity and density. Baroclinic velocity perturbations (u' , v') are calculated by subtracting the depth-averaged flow from the velocity perturbations, and baroclinic pressure perturbations are calculated by integrating the hydrostatic equation from the surface, $p' = p'_{\text{surf}} + \int_z^0 \rho' g dz$, where p'_{surf} is surface pressure perturbation due to the internal tide. p'_{surf} cannot be determined from the CTD measurements, so we apply the baroclinicity condition for pressure, i.e., $\int_{-H}^0 p' dz = 0$ [*Kunze et al.*, 2002]. *Gerkema and van Haren* [2007] argued that the baroclinicity condition for pressure is invalid over sloping topography. However, at this location, their suggestion of choosing the level $p' = 0$ based on the location of the strongest baroclinic currents in the water column yields energy flux profiles similar to those gained from applying the baroclinicity

condition. The depth-integrated internal tide energy flux is independent of p'_{surf} because the depth integral of \mathbf{u}' is zero by definition, i.e., $\int_{-H}^0 \mathbf{u}' dz = 0$ [*Ray and Mitchum*, 1997; *Cummins and Oey*, 1997]. Semidiurnal vertical isopycnal displacements are calculated from the M_2 harmonic fits to density, $\xi = -\rho'(d\bar{\rho}/dz)^{-1}$; then vertical velocity perturbations are inferred $w' = d\xi/dt$.

[26] The horizontal M_2 internal tide energy flux at the repeat station was concentrated in the main pycnocline (Figures 7b and 7c). The maximum across-slope energy flux (1.5 W m^{-2}) was at 595 m and directed up the slope. The maximum along-slope energy flux (2.5 W m^{-2}) was at 630 m and directed to the southwest. Above the pycnocline, the energy flux was $<0.25 \text{ W m}^{-2}$ in both directions. The depth-integrated internal tide energy flux was 140 W m^{-1} up-slope and 154 W m^{-1} along-slope to the southwest. Integrated through the pycnocline (550–650 m), the energy flux was 76 W m^{-1} up-slope and 112 W m^{-1} along-slope to the southwest.

[27] The vertical energy flux was of order one hundredth of the magnitude of the horizontal energy flux (Figure 7d). There was a convergence of internal tide energy in the pycnocline; between approximately 500 m and 600 m there was a downward flux of energy, while between 600 m and 650 m the energy flux was upward. At the top and the base of the pycnocline (550 m and 650 m) the energy flux was 10^{-3} W m^{-2} downward and $4 \times 10^{-3} \text{ W m}^{-2}$ upward, respectively. Above 500 m the energy flux was mostly downward and $<10^{-3} \text{ W m}^{-2}$.

5.2. Model Energy Flux

[28] For the model energy flux, semidiurnal baroclinic velocity perturbations are reconstructed from the M_2 harmonic constants. Baroclinic pressure perturbations are calculated $p' = p'_{\text{surf}} + \int_z^0 \rho N^2 \xi dz$, where N^2 is the initial stratification profile and vertical displacement (ξ) is inferred

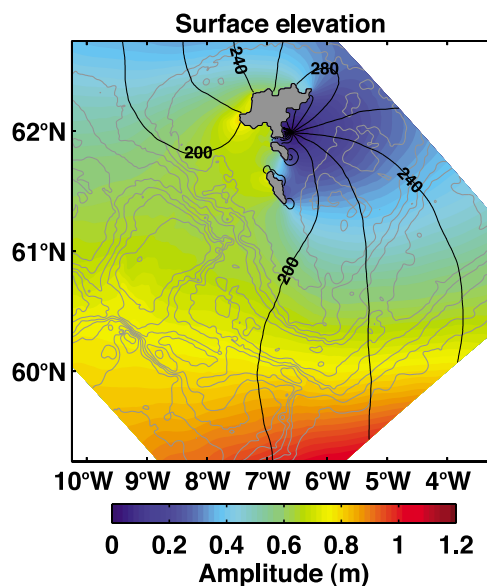


Figure 6. Cotidal plot of M_2 surface elevation amplitude (color) and phase (black contours) from the model. Greenwich phases are plotted with a 20° contour interval. The bathymetry contour interval is 200 m.

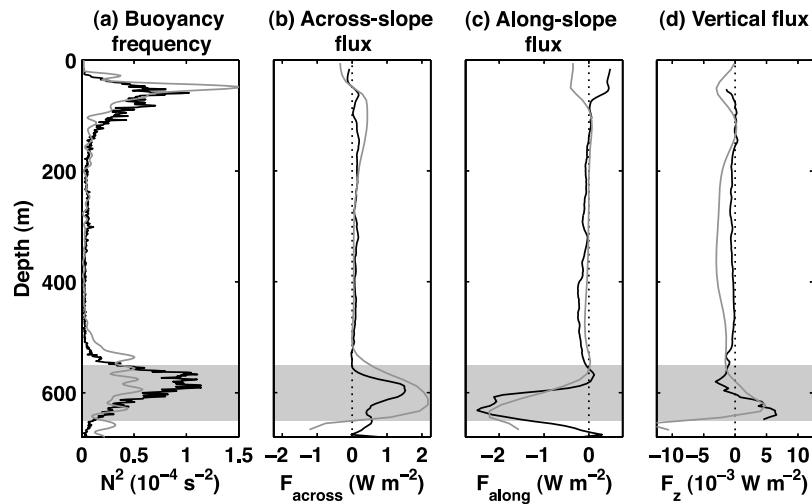


Figure 7. (a) Buoyancy frequency squared and (b) across-slope, (c) along-slope, and (d) vertical M_2 internal tide energy fluxes at the repeat station. The black lines are from the lowered ADCP/CTD measurements. The gray lines are from the model. Positive across-slope values are toward the southeast, and positive along-slope values are northeast. The shaded area is the location of the main pycnocline.

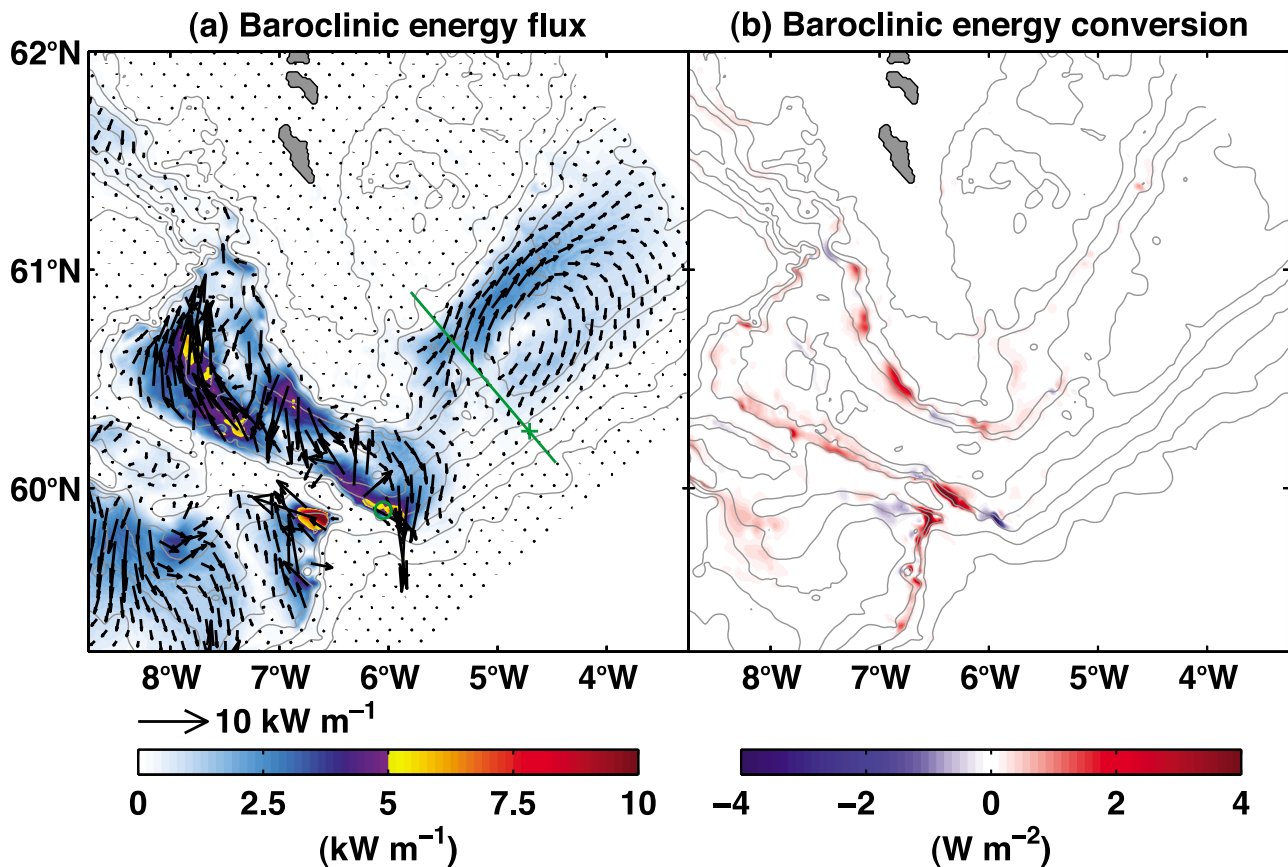


Figure 8. (a) Depth-integrated baroclinic M_2 energy flux from the model. Vectors are plotted every eight grid points (8 km) in each direction. The underlying color is the energy flux magnitude. The green cross is the location of the repeat station. The green line is the location of the across-channel section shown in Figure 9. The green circle at the southwestern end of the FSC is the location of the station where *Sherwin* [1991] observed an internal tide. (b) Barotropic-to-baroclinic M_2 energy conversion from the model. Positive values are sources of baroclinic energy. The bathymetry contour interval is 200 m.

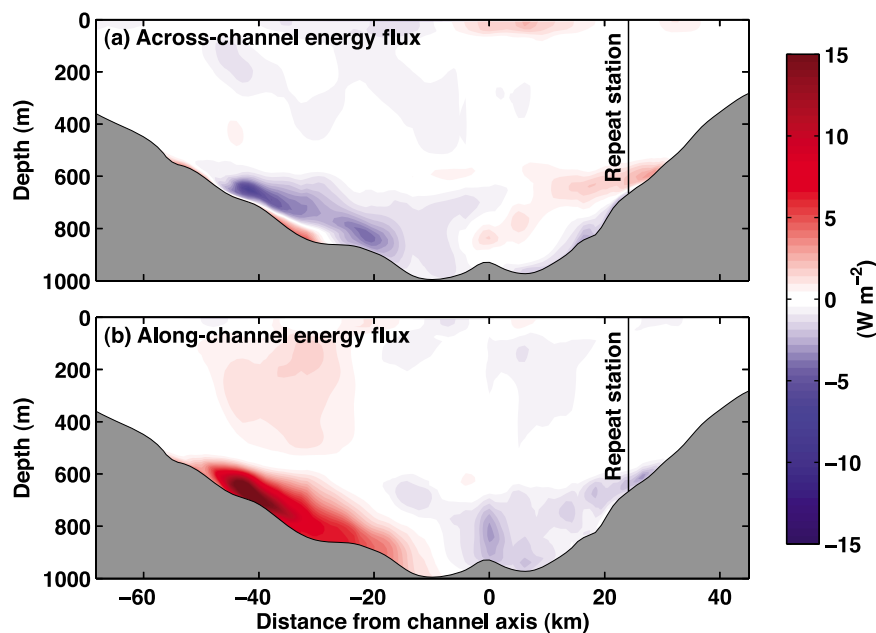


Figure 9. (a) Across-channel and (b) along-channel baroclinic M_2 energy flux at the across-channel section from the model. Positive across-slope values are toward the southeast, and positive along-slope values are northeast. The black line is the location of the repeat station.

from the vertical velocity perturbations. The baroclinicity condition is again used to constrain p'_{surf} .

[29] Barotropic-to-baroclinic energy conversion is calculated as $E_{\text{conv}} = \langle p'(-H)(\bar{\mathbf{u}} \cdot \mathbf{H}) \rangle$, where $\bar{\mathbf{u}}$ is barotropic velocity from the M_2 harmonic analysis output [Niwa and Hibiya, 2001]. Positive conversion indicates energy being transferred from the barotropic tide to the baroclinic tide. Negative conversion indicates work being done on the barotropic tide by the baroclinic tide [Zilberman *et al.*, 2009].

[30] Interpretation of internal tide energy fluxes in the FSC region is complicated by the existence of multiple generation sites. Rainville *et al.* [2010] showed that internal tides from multiple sources constructively and destructively interfere, resulting in depth-integrated energy flux beams appearing and disappearing in the open ocean. However, it is possible to make realistic inferences about internal tide generation by comparing depth-integrated baroclinic M_2 energy fluxes (Figure 8a) with the spatial distribution of barotropic-to-baroclinic M_2 energy conversion (Figure 8b). Although horizontally uniform, the model stratification is representative of the FSC and Wyville Thomson Basin, where we will focus our analysis. Stratification in the Rockall Trough is significantly weaker, therefore internal tide generation and propagation are unlikely to be accurate south of the Wyville Thomson Ridge.

[31] Large depth-integrated energy fluxes ($>5 \text{ kW m}^{-1}$) occur on the northern flank of the Wyville Thomson Ridge, directed northwest toward the Faroe Bank Channel. Along the shelf slope south of the Faroe Islands there is a southward energy flux, back toward the Wyville Thomson Ridge. The northern flank of the ridge and shelf slope south of the Faroes are areas of high ($>1 \text{ W m}^{-2}$) barotropic-to-baroclinic energy conversion so these energetic internal tides are most likely locally generated.

[32] At the southwestern end of the FSC, depth-integrated energy fluxes are spatially variable in both magnitude and direction. As suggested by Sherwin [1991], there is an internal tide radiating from the eastern end of the Wyville Thomson Ridge (where energy conversion is up to 4 W m^{-2}). However, the energy flux field suggests that internal tides generated along the shelf slope south of the Faroes cause constructive and destructive interference. At the location of the station where Sherwin [1991] observed an internal tide ($6^\circ 3' \text{W}$, $59^\circ 54' \text{W}$), the depth-integrated energy flux is 4.8 kW m^{-1} . This is close to the energy flux Sherwin [1991] estimated from the observations (4.7 kW m^{-1}). Maximum model vertical displacement at this location is 33 m, close to that observed by Sherwin [1991] (37 m).

[33] Further to the northeast, within the FSC, there is an order 2 kW m^{-1} depth-integrated energy flux beam that rotates clockwise. The beam likely originates on the Faroe slope as the appearance of depth-integrated energy fluxes are consistent with areas of barotropic-to-baroclinic energy conversion ($\sim 0.5 \text{ W m}^{-2}$). The energy flux is initially northeast, along the isobaths, before rotating clockwise within the channel and returning southwest along the West Shetland slope.

[34] The repeat station is located at the edge of the beam, close to where it disappears. The depth-integrated energy flux at this location is 204 W m^{-1} up-slope and 179 W m^{-1} along-slope to the southwest. Although these modeled energy fluxes are 15%–45% larger than the observed internal tide, they have a similar vertical structure with maxima in the main pycnocline (Figures 7b and 7c). Maximum model vertical displacement at the repeat station is 14 m, slightly larger than the observed M_2 vertical displacement of the pycnocline (9 m). The model overestimation of energy flux at this location is possibly due to the large spatial gradients in the modeled internal tide field. The

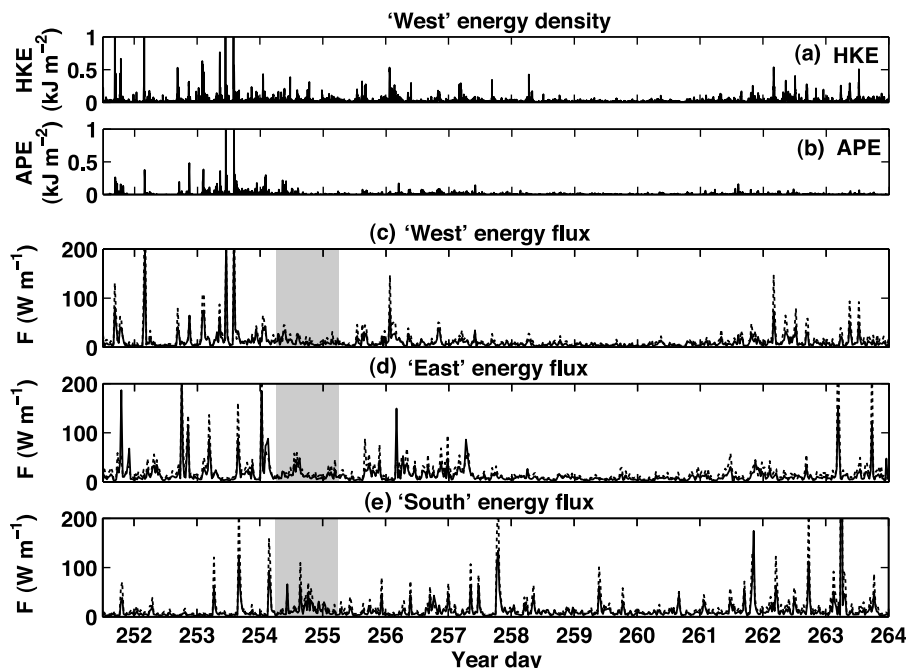


Figure 10. Nonlinear internal wave energy density from the “West” thermistor/ADCP mooring pair, integrated from the seabed to 50 m above the bottom: (a) horizontal kinetic energy density and (b) available potential energy density. Nonlinear internal wave energy flux from the (c) “West,” (d) “East,” and (e) “South” mooring pairs. The solid lines in Figures 10c–10e are from $F = c(\text{HKE} + \text{APE})$. The dashed lines are from $F = 2c(\text{HKE})$. The shaded area is the period the repeat station was occupied.

depth-integrated energy flux just 5 km up-slope of the repeat station is in good agreement with the observed internal tide.

[35] The depth-integrated energy flux beam is bisected by the across-channel section occupied during the slope mixing experiment. Across and along-channel energy fluxes at the section are shown in Figure 9. The across-channel energy flux is maximum below the main pycnocline (at 600 m), mostly directed toward the Faroe slope. However, over the West Shetland slope there is a middepth band of up-slope energy flux that is consistent with the up-slope energy flux in the pycnocline observed at the repeat station. The along-channel energy flux is larger than that across-channel and has a bimodal distribution below the pycnocline. Over the Faroe slope the energy flux is northeast while over the axis of the channel it is southwest, the start and end of the rotating beam. Above the pycnocline there are weaker energy fluxes in the same direction as those below.

6. Nonlinear Internal Wave Energy Flux

[36] The energy flux associated with the higher-frequency, nonlinear internal waves observed in the thermistor and ADCP mooring time series is estimated using the energy flux relation

$$F = c\langle \text{HKE} + \text{APE} \rangle, \quad (3)$$

where $\text{HKE} = \frac{1}{2}\rho u'u'$ is the horizontal kinetic energy density of the wave; $\text{APE} = \frac{1}{2}\rho N^2 \xi^2$ is the available potential energy density; and c is the wave velocity [Moum *et al.*, 2007]. u' and ξ are across-slope velocity perturbation and vertical isopycnal displacement, found by decomposing the velocity and density time series into time average values and anomalies,

i.e., $u' = u - \bar{u}$ and $\rho' = \rho - \bar{\rho}$. The time average values (\bar{u} and $\bar{\rho}$) are calculated using a 2 h running median. Using this method, $\bar{\rho}$ accurately follows the roughly semidiurnal across-slope advection of the dense water and removes it from the energy calculation. Relation (3) is used instead of $\langle \mathbf{u}'p' \rangle$ because the mooring array was designed to sample through the main pycnocline at high resolution so the overlying density structure and barotropic velocities were not measured. We consider only the up-slope energy flux for the nonlinear waves because the mean wave velocity (0.27 m s^{-1} , see section 3) was almost perpendicular to the isobaths. For each mooring pair, HKE and APE are integrated from the seabed up to 50 m above the bottom; then the wave-averaged energy flux calculated from (3) using 30 min time averages.

[37] The kinetic energy and available potential energy showed reasonable correlation (Figures 10a and 10b), with HKE generally larger than APE. There were periods where APE went to zero, but HKE was nonzero due to noise in the ADCP data. Comparing Figures 10a and 10b with Figure 3b, most large energy peaks coincided with the leading wave of a train or individual solitary waves. Instantaneous energies were occasionally $>1 \text{ kJ m}^{-2}$, but time average values for the three mooring pairs were of order 30 J m^{-2} for HKE and 10 J m^{-2} for APE.

[38] Using linear regression, $\langle \text{HKE} \rangle / \langle \text{APE} \rangle \simeq 3.3$ ($R^2 = 0.14$), a factor of 2 larger than previous observations of nonlinear internal waves. For bottom-trapped waves on the Oregon continental shelf, Klymak and Moum [2003] estimated the energy ratio to be 1.5 (revised by Moum *et al.* [2007]). A similar ratio was estimated for surface-trapped waves in the South China Sea [Klymak *et al.*, 2006]. However, more recent observations of bottom-trapped waves on the Oregon shelf

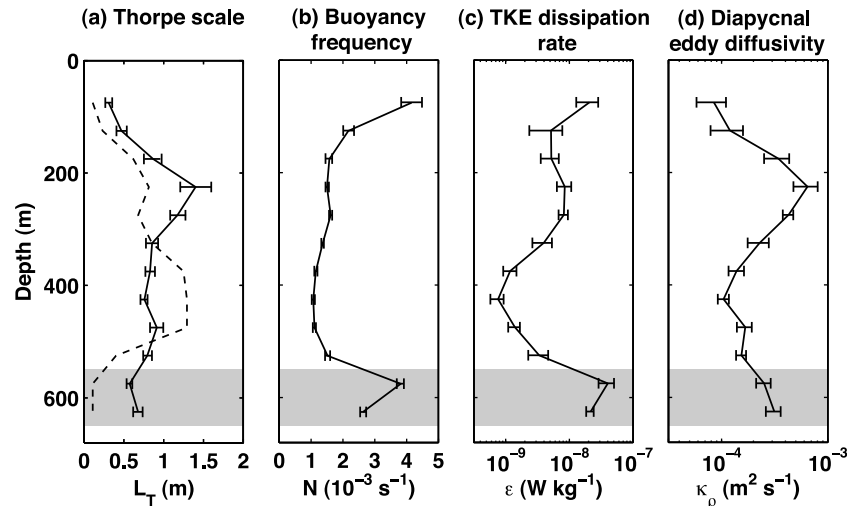


Figure 11. (a) Thorpe scale, (b) overturn-scale buoyancy frequency, (c) TKE dissipation rate, and (d) diapycnal eddy diffusivity at the repeat station in 50 m vertical bins and time-averaged over the 25 casts. The error bars show the standard error for each bin. The dashed line in Figure 11a is the overturn resolution limit of the CTD. The shaded area is the location of the main pycnocline.

by *Moum et al.* [2007] suggested equal partitioning of HKE and APE. The deviation from previous energy ratio estimates was likely due to underestimation of APE, resulting from the 50 m thermistor moorings not sampling the whole vertical extent of the waves. *Moum et al.* [2007] showed that for waves of elevation HKE is maximum near the bottom, while APE is elevated over a larger depth range. To estimate an upper bound, the nonlinear internal wave energy flux is recalculated assuming the energy ratio is one, i.e., $F = 2c\langle\text{HKE}\rangle$.

[39] Peak wave-averaged energy fluxes reached 200 W m^{-1} , but were typically of order 10 W m^{-1} (Figures 10c–10e). During the period the repeat station was occupied and estimates of turbulent mixing made (see section 7.1) the energy fluxes were small, but relatively constant. Mean values for this period were consistent between the three mooring pairs, $13.1 \pm 3.6 \text{ W m}^{-1}$ for the “West” moorings; $16.7 \pm 4.3 \text{ W m}^{-1}$ for the “East” moorings; and $17.8 \pm 5 \text{ W m}^{-1}$ for the “South” moorings. The uncertainty is the standard error between the 48 energy flux estimates during the 24 h period and includes the upper bound. Given the uncertainty, the three energy fluxes were not statistically different. Therefore, to infer the nonlinear internal wave dissipation rate (section 7.3), we estimated the energy flux in the bottom 50 m to be 10–20 W m^{-1} during the period the repeat station was occupied.

7. Internal Wave Dissipation and Mixing

[40] In this section, we consider where the internal waves are dissipated and the resulting turbulent mixing. Turbulent kinetic energy (TKE) dissipation rate and diapycnal eddy diffusivity are first estimated from Thorpe scale analysis of the CTD data. The former is then compared to bulk TKE dissipation rates inferred from the observed internal tide and nonlinear internal wave energy fluxes. Other sources of energy available for mixing are considered in the discussion.

7.1. Thorpe Scale

[41] In the absence of any direct turbulence measurements, TKE dissipation rate and diapycnal eddy diffusivity

are inferred from Thorpe scale analysis [*Thorpe*, 1977] of density overturns in the CTD profiles at the repeat station (Appendix A). The largest overturns occurred between 200 m and 250 m, where time average Thorpe scale, $\langle L_T \rangle$, reached 1.4 m (Figure 11). Between 350 m and 500 m, $\langle L_T \rangle$ was shorter than the overturn resolution limit of the CTD so was likely dominated by instrument noise. However, in the main pycnocline $\langle L_T \rangle$ was ~ 0.6 m, significantly longer than resolution limit in strong stratification (0.11 m). TKE dissipation rate was highest in the pycnocline due to its sensitivity to N , reaching $4 \times 10^{-8} \text{ W kg}^{-1}$. Diapycnal eddy diffusivity was maximum at the same depth as $\langle L_T \rangle$, below the seasonal thermocline, and reached $6 \times 10^{-4} \text{ m}^2 \text{ s}^{-1}$.

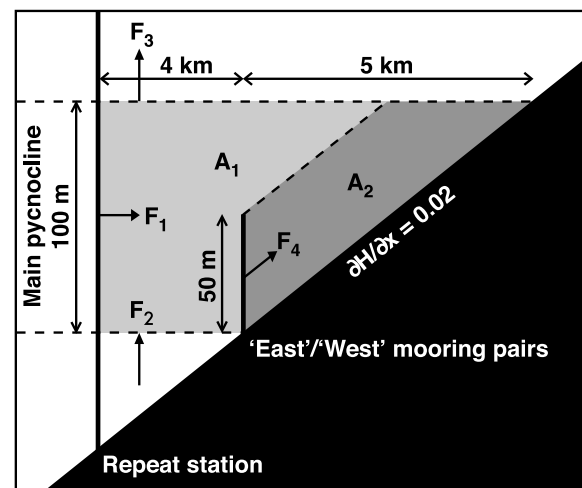


Figure 12. Schematic of internal wave energy dissipation. For the internal tide the net energy flux into the region of dissipation is $F_{\text{net}} = F_1 + F_2 - F_3$, and the area of the region is $A_1 = 100 \text{ m} \times 4000 \text{ m} + 100 \text{ m} \times 5000 \text{ m} \times 1/2$. For the nonlinear internal waves the net energy flux is $F_{\text{net}} = F_4$, and the area is $A_2 = 50 \text{ m} \times 5000 \text{ m} \times 3/4$.

[42] Averaged through the pycnocline (550–650 m), TKE dissipation rate was $3 \times 10^{-8} \text{ W kg}^{-1}$ and diapycnal eddy diffusivity $3 \times 10^{-4} \text{ m}^2 \text{ s}^{-1}$. The latter was an order of magnitude larger than typical values for the interior of the open ocean [Ledwell *et al.*, 1993; Toole *et al.*, 1994], but of the same order as measured over rough abyssal topography [Polzin *et al.*, 1997; Ledwell *et al.*, 2000] and seamounts [Toole *et al.*, 1997; Eriksen, 1998].

7.2. Internal Tide Dissipation

[43] The across-slope component of the M_2 internal tide energy flux at the repeat station was up-slope in the main pycnocline, however, the pycnocline intersected the shelf slope less than 10 km up-slope from the location to the repeat station. We therefore make the assumption that all the up-slope M_2 internal tide energy in the pycnocline was dissipated in a region bounded by the repeat station, the shelf slope, and the top and base of the pycnocline (Figure 12). The bulk TKE dissipation rate in this region is estimated

$$\epsilon_{\text{bulk}} \simeq F_{\text{net}}/[\rho A(1 + \Gamma)], \quad (4)$$

where F_{net} is the net energy flux into the region and A is the across-slope sectional area of the region. Γ is the mixing efficiency, assumed to be 0.2 [Oakey, 1982].

[44] From the internal tide observations, the net energy flux was 101 W m^{-1} , including the vertical fluxes at the base and top of the pycnocline (25 W m^{-1}). The across-slope sectional area of the dissipation region is estimated to be $6.5 \times 10^5 \text{ m}^2$ for a pycnocline thickness of 100 m and the measured slope gradient, 0.02 (Figure 12). This yields a bulk TKE dissipation rate for the internal tide of $1.3 \times 10^{-7} \text{ W kg}^{-1}$, a factor of 4 larger than the dissipation rate in the pycnocline inferred from Thorpe scale analysis ($3 \times 10^{-8} \text{ W kg}^{-1}$).

[45] The assumption that all the energy in the pycnocline was dissipated on the slope may not completely hold because the West Shetland slope is supercritical to semidiurnal internal tides where it is intersected by the pycnocline. Using equation (1) and taking N to be the mean buoyancy frequency in the lower 50 m of the water column along the across-channel section, the slope was subcritical to the M_2 internal tide below the 770 m isobath and above the 480 m isobath. Between these isobaths the slope was supercritical. This variation with depth implies that, in the pycnocline, reflection of internal tide energy back into the channel will occur, while above and below the pycnocline, energy will continue to propagate onto the shelf. However, some internal tide energy will be dissipated in the bands of near-critical slope between the subcritical and supercritical areas. The bulk dissipation rate inferred from the internal tide energy flux should therefore be considered an upper bound.

[46] Considering the factor of 3 error in the estimation of TKE dissipation rate from Thorpe scale analysis [Fer *et al.*, 2004], and taking the bulk dissipation rate to be an upper bound, the comparison is encouraging. The slight overestimation of dissipation rate inferred from the internal tide energy flux suggests that either (1) only a fraction of the internal tide energy was dissipated on the slope, with the remainder being reflected back into the channel, or (2) the dissipation estimate is low, either because some large overturns were missed, or the observations were not made where the most intense dissipation occurred. Estimation of the frac-

tions of internal tide energy dissipated on the slope and reflected back into the channel is the subject of ongoing research.

7.3. Nonlinear Internal Wave Dissipation

[47] The higher-frequency, nonlinear internal waves were bottom-trapped so must have dissipated or broken in the area the pycnocline intersected the shelf slope because the near-bed buoyancy frequency further up-slope was less than the frequency of the waves. We therefore make a similar assumption as for the internal tide, that all the up-slope nonlinear internal wave energy was dissipated in a region bounded by the “East” and “West” mooring pairs, the shelf slope, and the top of the pycnocline (Figure 12).

[48] During the period the repeat station was occupied, the energy flux associated with the nonlinear internal waves was smaller than that for the internal tide, only $10\text{--}20 \text{ W m}^{-1}$. However, the across-slope sectional area of the dissipation region is also estimated to be smaller, $1.9 \times 10^5 \text{ m}^2$, because the “East” and “West” mooring pairs were further up the slope than the repeat station (Figure 12). This yields a bulk TKE dissipation rate for the nonlinear internal waves of $4.3\text{--}8.5 \times 10^{-8} \text{ W kg}^{-1}$, roughly half that for the internal tide and slightly larger than the dissipation rate inferred from Thorpe scale analysis.

8. Discussion and Summary

[49] The role of internal tides and nonlinear internal wave trains in transferring energy through the FSC and sustaining the high level of mixing on the West Shetland slope is now discussed. Other sources of energy available for mixing and the global context are also considered.

8.1. Internal Tides in the Faroe-Shetland Channel

[50] The order 10 m amplitude semidiurnal internal tide observed at the repeat station was not typical of the FSC as a whole. Both the M_2 amplitude and energy flux were smaller than observed by Sherwin [1991] at the southwestern end of the channel, the latter by over an order of magnitude. The model results suggest that the M_2 internal tide in the channel is generated at multiple sites, not just at the Wyville Thomson Ridge as suggested by Sherwin [1991]. At the location of the repeat station, baroclinic variability is dominated by an internal tide beam that likely originates on the Faroe slope. The area of low energy flux between the Wyville Thomson Ridge and the repeat station suggests that there is destructive interference between the beam and the internal tide generated at the ridge.

[51] The bulk TKE dissipation rate inferred from the observed internal tide energy flux was a factor of 4 larger than that inferred from Thorpe scale analysis. Supercritical reflection of the internal tide in the main pycnocline may explain the overestimation and suggests that the assumption that all the energy in the pycnocline was dissipated on the slope does not completely hold. The high level of mixing on the slope can be accounted for by the internal tide, even if the majority of the energy was reflected.

[52] Modeled internal tide energy fluxes on the northern flank of the Wyville Thomson Ridge are over an order of magnitude larger than at the location of the repeat station, $>5 \text{ kW m}^{-1}$. These are comparable to the depth-integrated baroclinic M_2 energy fluxes produced by the model at the

Hawaiian Ridge [Carter *et al.*, 2008], known to be a region of energetic internal tide generation. However, the internal tide does not propagate away from the Wyville Thomson Ridge in beams as at the Hawaiian Ridge, instead the energy is trapped in the Wyville Thomson Basin and must be dissipated locally. High TKE dissipation rates (up to 10^{-5} W kg^{-1}) have been measured in the basin using a microstructure profiler (E. J. Venables, personal communication, 2010) and inferred from Thorpe scale analysis of CTD data [Mauritzen *et al.*, 2005].

8.2. Nonlinear Internal Wave Trains

[53] The trains of near-bed nonlinear internal waves observed in the mooring time series were likely generated some distance from the site of the slope mixing experiment because they were rank ordered. The generation site must have been offshore, rather than on the shelf, because the wave trains were observed to propagate up the slope. As the wave trains occurred in the mooring time series at roughly semidiurnal intervals, they were likely tidally forced and may have been a nonlinear manifestation of the internal tide, as speculated by Sherwin [1991].

[54] The bulk TKE dissipation rate inferred from the nonlinear internal wave energy flux was roughly half that inferred from the internal tide energy flux, and slightly larger than that inferred from Thorpe scale analysis. However, unlike the internal tide, which is a constant source of energy for mixing on the slope, the nonlinear internal wave energy flux was intermittent. Although typically energy fluxes were only of order 10 W m^{-1} , energy fluxes up to 200 W m^{-1} were occasionally observed. These were comparable to the depth-integrated internal tide energy flux, yet were contained within the bottom 50 m. Dissipation of these peak energy fluxes on the slope implies occasional bulk TKE dissipation rates an order of magnitude larger than those inferred here for the period the repeat station was occupied. During these peak energy events, dissipation of the wave trains was likely to have caused more mixing on the slope than the linear internal tide.

8.3. Other Sources of Mixing Energy

[55] The internal tide and nonlinear internal wave energy fluxes were sufficient to sustain the high levels of mixing on the slope, even if the majority of the internal tide energy was reflected. In this section, two other sources of energy available for mixing are considered: turbulence at the seabed from the work of bottom friction on barotropic tidal currents, and mechanical forcing at the surface by the wind.

[56] The work of bottom friction on barotropic tidal currents generates TKE in the bottom boundary layer. Using $D = \rho C_d \langle \mathbf{u}^3 \rangle$, where \mathbf{u} is barotropic velocity from the full-depth lowered ADCP profiles at the repeat station and $C_d = 0.0025$ is the drag coefficient, we estimate the source of TKE at the bottom boundary to have been ~ 0.002 W m^{-2} . Assuming the TKE penetrated upward no further than 150 m (the top of the main pycnocline), the barotropic tide can account for a dissipation rate of 1.2×10^{-8} W kg^{-1} . This is a factor of 2 smaller than the TKE dissipation rate in the pycnocline inferred from Thorpe scale analysis and an order of magnitude smaller than the bulk dissipation rate inferred from the internal tide energy flux. If this assumption is relaxed, allowing the TKE generated at the bottom boundary to pene-

trate further through the water column, the dissipation rate that can be accounted for by the barotropic tide is even less.

[57] The input of TKE to the ocean by wind forcing, $W = \langle \tau \mathbf{u}_g \rangle$, where τ is wind stress and \mathbf{u}_g is surface geostrophic velocity, is typically 0.01 W m^{-2} [Huthnance, 1995]. This estimate assumes all the forced small-scale motions are dissipated within the surface mixed layer and do not contribute to mixing in the pycnocline. Energy from wind forcing can be transported below the surface mixed layer by near-inertial internal waves. These downward propagating waves are a significant input of energy to the global ocean [Alford, 2003], comparable to tidal energy dissipation in the deep ocean [Egbert and Ray, 2000] and the work done by the wind on the general circulation [Wunsch, 1998]. However, at this location, they are discounted as a significant source of energy for mixing because spectral analysis of the moored ADCPs data (not shown) showed little variance at near-inertial and subinertial frequencies.

8.4. Global Context

[58] The internal tide energy flux observed on the West Shetland slope was small compared that observed in other regions. For example, the Hawaii Ocean Mixing Experiment found the internal tide energy flux away from the crest of the Hawaiian Ridge to be 5 to 6 kW m^{-1} [Nash *et al.*, 2006] and ~ 16 kW m^{-1} across the 3000 m isobath [Lee *et al.*, 2006]. Other estimates of internal tide energy flux include 5 kW m^{-1} at the mouth of Monterey Submarine Canyon off California [Kunze *et al.*, 2002], 1 kW m^{-1} on the continental slope off Virginia [Nash *et al.*, 2004], 2.4 kW m^{-1} away from Great Meteor Seamount [Gerkema and van Haren, 2007], order 1 kW m^{-1} on the Oregon continental slope [Nash *et al.*, 2007], and 14 kW m^{-1} at the mouth of Gaoping Canyon off Taiwan [Lee *et al.*, 2009]. The observed energy flux was however comparable to estimates at the European shelf edge (e.g., 104 W m^{-1} west of Scotland [Sherwin, 1988] and 100 – 200 W m^{-1} in the Celtic Sea [Green *et al.*, 2008]), although larger energy fluxes occur at shelf breaks elsewhere [Holloway, 1984; Huthnance, 1989].

[59] Although small, the majority of the energy flux on the West Shetland slope was contained within the main pycnocline, where large property gradients exist. Turbulent mixing resulting from dissipation of the internal tide on the slope will therefore be effective in the vertical transport of heat, salt, and nutrients.

[60] In contrast to the small energy flux on the West Shetland slope, the modeled internal tide energy fluxes on the northern flank of the Wyville Thomson Ridge are comparable to the largest of the observed energy fluxes quoted above, suggesting that the ridge may be a globally significant source of internal tide energy. Moreover, the internal tide does not propagate far from ridge so all the energy must be dissipated in the Wyville Thomson Basin, between the FSC and Faroe Bank Channel. High levels of internal tide induced mixing in the basin are likely to modify the θ - S properties of the deep water overflowing the Greenland-Scotland Ridge through the channels, potentially affecting large-scale ocean circulation.

8.5. Summary

[61] Model results suggest that the internal tide in the FSC is generated at multiple sites, including the Wyville

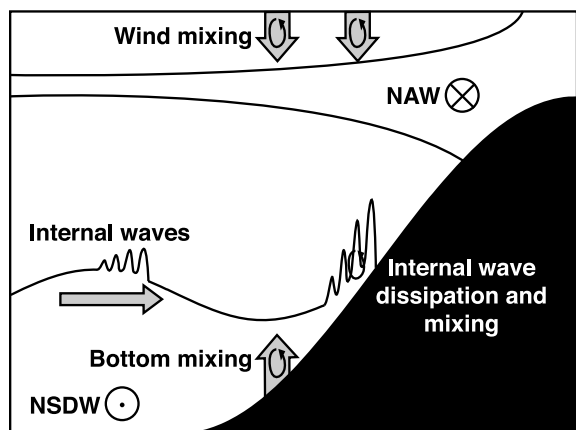


Figure 13. Schematic of internal waves and mixing processes that occur on the West Shetland slope. Mechanical forcing by the wind mixes the surface layer. Turbulence from the work of bottom friction on barotropic tidal currents mixes the bottom boundary layer. Internal waves propagate along the main pycnocline and dissipate on the slope, causing local mixing in the pycnocline.

Thomson Ridge and the Faroe slope. During the slope mixing experiment on the West Shetland slope, the internal tide energy flux was onshore, concentrated in the main pycnocline, and sufficient to sustain high levels of mixing where the pycnocline met the slope (Figure 13), even if the majority of the energy was reflected. Nonlinear internal wave trains propagated up the slope and may have been a nonlinear manifestation of the internal tide. During energetic periods the wave trains were likely to have caused more mixing on the slope than the linear internal tide.

Appendix A: Thorpe Scale Analysis

[62] TKE dissipation rate (ϵ) and diapycnal eddy diffusivity (κ_ρ) are inferred from the CTD data using Thorpe scale analysis [Thorpe, 1977]. The potential density samples in each profile are reordered so that the profiles are statically stable. The vertical distance the samples are moved during the reordering process is the Thorpe displacement and the Thorpe scale (L_T) is the RMS Thorpe displacement over each complete overturn.

[63] TKE dissipation rate is then estimated by relating the Ozmidov scale, $L_O = (\epsilon/N^3)^{1/2}$ [Ozmidov, 1965], to the Thorpe scale by the empirical relation $L_O = 0.8 L_T$ [Dillon, 1982], giving

$$\epsilon = 0.64 L_T^2 N^3, \quad (\text{A1})$$

where N is the buoyancy frequency over the depth range of the overturn. Diapycnal eddy diffusivity is related to TKE dissipation rate by $\kappa_\rho = \Gamma \epsilon / N^2$ [Osborn, 1980], so can be estimated from L_T using the relation

$$\kappa_\rho \approx 0.1 L_T^2 N, \quad (\text{A2})$$

assuming a mixing efficiency of 0.2 [Oakey, 1982].

[64] The Thorpe displacement resolution of the CTD is calculated following Stansfield *et al.* [2001] and is depth dependent, varying in part with the background density gradient. In the main pycnocline and seasonal thermocline, where $N^2 > 3.5 \times 10^{-5} \text{ s}^{-2}$, the length scale of the smallest resolvable overturns is determined by the depth resolution of the instrument (0.11 m). Elsewhere in the water column, where the density gradient is small, density resolution (0.0004 kg m^{-3}) limits overturn resolution to as long as 1.3 m (Figure 11a). Thorpe scales shorter than the resolution limit are disregarded because they are likely to be dominated by instrument noise.

[65] The problems associated with ship heave were minimized by first removing pressure reversals, then flagging sections of casts with frequent pressure reversals or rapid changes in descent rate. Approximately 20% of the observational record was removed as a result. Differences between the temperature and conductivity sensor response times and the thermal lag of the conductivity cell were corrected for during processing [Lueck and Picklo, 1990; Morison *et al.*, 1994].

[66] In order to determine if density inversions are real turbulent overturns rather than instrument noise, a “run-length” test is applied to each overturn [Galbraith and Kelley, 1996]. Run length (n) is the number of sequential Thorpe displacements of the same sign. An overturn is assumed real if the RMS run length through the overturning region is longer than the RMS run length expected for a random uncorrelated time series, $(\sum_1^\infty 2^{-n} n^2)^{1/2} = \sqrt{6}$, following Timmermans *et al.* [2003]. In strongly stratified regions, where the noise amplitude is comparable to the average density difference between consecutive measurements, the expected RMS run length has been shown to be shorter than $\sqrt{6}$ [Johnson and Garrett, 2004]. As a result, this method may reject some small, but real, turbulent overturns in the main pycnocline, potentially overestimating L_T .

[67] The Thorpe scale is calculated for each overturn that passes the run length test then ϵ and κ_ρ inferred from relations (A1) and (A2). For each of the 25 casts at the repeat station, L_T , N , ϵ , and κ_ρ are averaged in 50 m vertical bins. The time average and standard error (standard deviation divided by the square root of the number of casts) are then calculated for each bin (Figure 11). Other uncertainties in the calculation of ϵ and κ_ρ arise from the accuracy of the CTD and variability in the empirical constants. Including these additional sources of error, ϵ can be estimated within a factor of 3 and κ_ρ within a factor of 4 [Fer *et al.*, 2004].

[68] **Acknowledgments.** R. A. Hall was supported by a Natural Environment Research Council Ph.D. studentship, NER/S/A/2005/13812. The cooperation of the master and crew of the FS *Poseidon* (IFM-GEOMAR) and the loan of the lowered ADCP by Bogi Hansen (Faroese Fisheries Laboratory) are gratefully acknowledged. Assistance with the setup and running of the numerical model was provided by Glenn Carter (University of Hawaii). Helpful comments on the manuscript were provided by two reviewers.

References

- Alford, M. H. (2003), Improved global maps and 54-year history of wind-work on ocean inertial motions, *Geophys. Res. Lett.*, *30*(8), 1424, doi:10.1029/2002GL016614.
- Apel, J. R., J. R. Holbrook, A. K. Liu, and J. J. Tsai (1985), The Sulu Sea internal soliton experiment, *J. Phys. Oceanogr.*, *15*, 1625–1651.
- Baines, P. G. (1982), On internal tide generation models, *Deep Sea Res.*, *29*, 307–338.

- Blumberg, A. F., and G. L. Mellor (1987), A description of a three-dimensional coastal ocean circulation model, in *Three-Dimensional Coastal Ocean Models, Coastal and Estuarine Sci. Ser.*, vol. 4, edited by N. S. Heaps, pp. 1–16, AGU, Washington, D. C.
- Borenäs, K., and P. Lundberg (2004), The Faroe-Bank Channel deep-water overflow, *Deep Sea Res., Part II*, *51*, 335–350.
- Borenäs, K. M., I. L. Lake, and P. A. Lundberg (2001), On the intermediate water masses of the Faroe-Bank Channel overflow, *J. Phys. Oceanogr.*, *31*, 1904–1914.
- Carter, G. S. (2010), Barotropic and baroclinic M_2 tides in the Monterey Bay region, *J. Phys. Oceanogr.*, *40*, 1766–1783.
- Carter, G. S., and M. A. Merrifield (2007), Open boundary conditions for regional tidal simulations, *Ocean Modell.*, *18*, 194–209.
- Carter, G. S., M. C. Gregg, and R.-C. Lien (2005), Internal waves, solitary-like waves, and mixing on the Monterey Bay shelf, *Cont. Shelf Res.*, *25*, 1499–1520.
- Carter, G. S., M. A. Merrifield, J. M. Becker, K. Katsumata, M. C. Gregg, D. S. Luther, M. D. Levine, T. J. Boyd, and Y. L. Firing (2008), Energetics of M_2 barotropic-to-baroclinic tidal conversion at the Hawaiian Islands, *J. Phys. Oceanogr.*, *38*, 2205–2223.
- Cummins, P. F., and L.-Y. Oey (1997), Simulation of barotropic and baroclinic internal tides of northern British Columbia, *J. Phys. Oceanogr.*, *27*, 762–781.
- Davies, A. M., S. C. M. Kwong, and J. C. Lee (2001), A detailed comparison of a range of three-dimensional models of the M_2 tide in the Faeroe-Shetland Channel and northern North Sea, *J. Phys. Oceanogr.*, *31*, 1747–1763.
- Dickson, R. R., and J. Brown (1994), The production of North Atlantic Deep Water: Sources, rates, and pathways, *J. Geophys. Res.*, *99*, 12,319–12,341.
- Dillon, T. M. (1982), Vertical overturns: A comparison of Thorpe and Ozmidov scales, *J. Geophys. Res.*, *87*, 9601–9613.
- Egbert, G. D. (1997), Tidal data inversion: Interpolation and interference, *Prog. Oceanogr.*, *40*, 53–80.
- Egbert, G. D., and S. Y. Erofeeva (2002), Efficient inverse modeling of barotropic ocean tides, *J. Atmos. Oceanic Technol.*, *19*, 183–204.
- Egbert, G. D., and R. D. Ray (2000), Significant dissipation of tidal energy in the deep ocean inferred from satellite altimeter data, *Nature*, *405*, 775–778.
- Eriksen, C. C. (1998), Internal wave reflection and mixing at Fieberling Guyot, *J. Geophys. Res.*, *103*, 2977–2994.
- Fer, I., R. Skogseth, and P. M. Haugan (2004), Mixing of the Storfjorden overflow (Svalbard Archipelago) inferred from density overturns, *J. Geophys. Res.*, *109*, C01005, doi:10.1029/2003JC001968.
- Flather, R. A. (1976), A tidal model of the north-west European continental shelf, *Mem. Soc. R. Sci. Liege*, *6*, 141–164.
- Galbraith, P. S., and D. E. Kelley (1996), Identifying overturns in CTD profiles, *J. Atmos. Oceanic Technol.*, *13*, 688–702.
- Gerkema, T. (1996), A unified model for the generation and fission of internal waves in a rotating ocean, *J. Mar. Res.*, *54*, 421–450.
- Gerkema, T. (2002), Application of an internal tide generation model to baroclinic spring-neap cycles, *J. Geophys. Res.*, *107*(C9), 3124, doi:10.1029/2001JC001177.
- Gerkema, T., and H. van Haren (2007), Internal tides and energy fluxes over Great Meteor Seamount, *Ocean Sci.*, *3*, 441–449.
- Gerkema, T., and J. T. F. Zimmerman (1995), Generation of nonlinear tides and solitary waves, *J. Phys. Oceanogr.*, *25*, 1081–1094.
- Green, J. A., J. H. Simpson, S. Legg, and M. R. Palmer (2008), Internal waves, baroclinic energy fluxes and mixing at the European shelf edge, *Cont. Shelf Res.*, *28*, 937–950.
- Hall, R. A., and G. S. Carter (2011), Internal tides in Monterey Submarine Canyon, *J. Phys. Oceanogr.*, *41*, 186–204.
- Haney, R. L. (1991), On the pressure gradient force over steep topography in sigma coordinate ocean models, *J. Phys. Oceanogr.*, *21*, 610–619.
- Hansen, B., and S. Østerhus (2000), North Atlantic–Nordic Seas exchanges, *Prog. Oceanogr.*, *45*, 109–208.
- Henry, F. S., and A. Hoering (1997), Energetics of borelike internal waves, *J. Geophys. Res.*, *102*, 3323–3330.
- Holloway, P. E. (1984), On the semidiurnal internal tide at a shelf-break region on the Australian North West Shelf, *J. Phys. Oceanogr.*, *14*, 1787–1799.
- Holloway, P. E. (1987), Internal hydraulic jumps and solitons at a shelf break region on the Australian North West Shelf, *J. Geophys. Res.*, *92*, 5405–5416.
- Hosegood, P., and H. van Haren (2004), Near-bed solibores over the continental slope in the Faeroe-Shetland Channel, *Deep Sea Res., Part II*, *51*, 2943–2971.
- Hosegood, P., H. van Haren, and C. Veth (2005), Mixing in the interior of the Faeroe-Shetland Channel, *J. Mar. Res.*, *63*, 529–561.
- Huthnance, J. M. (1989), Internal tides and waves near the continental shelf edge, *Geophys. Astrophys. Fluid Dyn.*, *48*, 81–106.
- Huthnance, J. M. (1995), Circulation, exchange and water masses at the ocean margin: The role of physical processes at the shelf edge, *Prog. Oceanogr.*, *35*, 353–431.
- Johnson, H. L., and C. Garrett (2004), Effects of noise on Thorpe scales and run lengths, *J. Phys. Oceanogr.*, *34*, 2359–2372.
- Klymak, J. M., and J. N. Moum (2003), Internal solitary waves of elevation advancing on a shoaling shelf, *Geophys. Res. Lett.*, *30*(20), 2045, doi:10.1029/2003GL017706.
- Klymak, J. M., R. Pinkel, C.-T. Lui, A. K. Liu, and D. Laura (2006), Prototypical solitons in the South China Sea, *Geophys. Res. Lett.*, *33*, L11607, doi:10.1029/2006GL025932.
- Kunze, E., L. K. Rosenfeld, G. S. Carter, and M. C. Gregg (2002), Internal waves in Monterey Submarine Canyon, *J. Phys. Oceanogr.*, *32*, 1890–1913.
- Kwong, S. C. M., and A. M. Davies (2001), A three dimensional model of the M_2 , S_2 , N_2 , K_1 , and O_1 tides in the Faeroe-Shetland Channel, *Cont. Shelf Res.*, *21*, 1263–1297.
- Ledwell, J. R., A. J. Watson, and C. S. Law (1993), Evidence for slow mixing across the pycnocline from an open-ocean tracer-release experiment, *Nature*, *364*, 701–703.
- Ledwell, J. R., E. T. Montgomery, K. L. Polzin, L. C. St. Laurent, R. W. Schmitt, and J. M. Toole (2000), Evidence for enhanced mixing over rough topography in the abyssal ocean, *Nature*, *403*, 179–182.
- Lee, C. M., E. Kunze, T. B. Sanford, J. D. Nash, M. A. Merrifield, and P. E. Holloway (2006), Internal tides and turbulence along the 3000-m isobath of the Hawaiian Ridge, *J. Phys. Oceanogr.*, *36*, 1165–1182.
- Lee, I.-H., R.-C. Lien, J. T. Liu, and W.-S. Chuang (2009), Turbulent mixing and internal tides in Gaoping (Kaoping) Submarine Canyon, Taiwan, *J. Mar. Syst.*, *76*, 383–396.
- Lueck, R. G., and J. J. Picklo (1990), Thermal inertia of conductivity cells: Observations with a Sea-Bird cell, *J. Atmos. Oceanic Technol.*, *7*, 756–768.
- Mauritzen, C., J. Price, T. Sanford, and D. Torres (2005), Circulation and mixing in the Faeroese Channels, *Deep Sea Res., Part I*, *52*, 883–913.
- Mellor, G. L., and T. Yamada (1982), Development of a turbulence closure model for geophysical fluid problems, *Rev. Geophys.*, *20*, 851–875.
- Mellor, G. L., T. Ezer, and L.-Y. Oey (1994), The pressure gradient conundrum of sigma coordinate models, *J. Atmos. Oceanic Technol.*, *11*, 1126–1134.
- Morison, J., R. Anderson, N. Larson, E. D’Asaro, and T. Boyd (1994), The correction for thermal-lag effects in Sea-Bird CTD data, *J. Atmos. Oceanic Technol.*, *11*, 1151–1164.
- Moum, J. N., J. M. Klymak, J. D. Nash, A. Perlin, and W. D. Smyth (2007), Energy transport by nonlinear internal waves, *J. Phys. Oceanogr.*, *37*, 1968–1988.
- Nash, J. D., E. Kunze, J. M. Toole, and R. W. Schmitt (2004), Internal tide reflection and turbulent mixing on the continental slope, *J. Phys. Oceanogr.*, *34*, 1117–1134.
- Nash, J. D., M. H. Alford, and E. Kunze (2005), Estimating internal wave energy fluxes in the ocean, *J. Atmos. Oceanic Technol.*, *22*, 1551–1570.
- Nash, J. D., E. Kunze, C. M. Lee, and T. B. Sanford (2006), Structure of the baroclinic tide generated at Kaena Ridge, Hawaii, *J. Phys. Oceanogr.*, *36*, 1123–1135.
- Nash, J. D., M. H. Alford, E. Kunze, K. Martini, and S. Kelly (2007), Hot-spots of deep ocean mixing on the Oregon continental slope, *Geophys. Res. Lett.*, *34*, L01605, doi:10.1029/2006GL028170.
- New, A. L., and R. D. Pingree (1990), Evidence for internal tidal mixing near the shelf break in the Bay of Biscay, *Deep Sea Res.*, *37*, 1783–1803.
- Niwa, Y., and T. Hibiya (2001), Numerical study of the spatial distribution of the M_2 internal tide in the Pacific Ocean, *J. Geophys. Res.*, *106*, 22,441–22,449.
- Oakey, N. S. (1982), Determination of the rate of dissipation of turbulent energy from simultaneous temperature and velocity shear microstructure measurements, *J. Phys. Oceanogr.*, *12*, 256–271.
- Osborn, T. R. (1980), Estimates of the local rate of vertical diffusion from dissipation measurements, *J. Phys. Oceanogr.*, *10*, 83–89.
- Ostrovsky, L. A., and Y. A. Stepanyants (1989), Do internal solitons exist in the ocean?, *Rev. Geophys.*, *27*, 293–310.
- Ozmidov, R. V. (1965), On the turbulent exchange in a stably stratified ocean, *Izv. Acad. Sci. USSR Atmos. Oceanic Phys., Engl. Transl.*, *8*, 853–860.
- Pingree, R. D., G. T. Mardell, and A. L. New (1986), Propagation of internal tides from the upper slopes of the Bay of Biscay, *Nature*, *321*, 154–158.
- Polzin, K. L., J. M. Toole, J. R. Ledwell, and R. W. Schmitt (1997), Spatial variability of turbulent mixing in the abyssal ocean, *Science*, *276*, 93–96.
- Rainville, L., T. M. S. Johnston, G. S. Carter, M. A. Merrifield, R. Pinkel, P. F. Worcester, and B. D. Dushaw (2010), Interference pattern and propagation of the M_2 internal tide south of the Hawaiian Ridge, *J. Phys. Oceanogr.*, *40*, 311–325.
- Ray, R. D., and G. T. Mitchum (1997), Surface manifestations of internal tides in the deep ocean: Observations from altimetry and island gauges, *Prog. Oceanogr.*, *40*, 135–162.

- Sandstrom, H., and N. S. Oakey (1995), Dissipation in internal tides and solitary waves, *J. Phys. Oceanogr.*, *25*, 604–614.
- Saunders, P. M. (1990), Cold outflow from the Faroe Bank Channel, *J. Phys. Oceanogr.*, *20*, 29–43.
- Sherwin, T. J. (1988), Analysis of an internal tide observed on the Malin Shelf, north of Ireland, *J. Phys. Oceanogr.*, *18*, 1035–1050.
- Sherwin, T. J. (1991), Evidence of a deep internal tide in the Faeroe-Shetland channel, in *Tidal Hydrodynamics*, edited by B. B. Parker, pp. 469–488, John Wiley, New York.
- Sherwin, T. J., C. R. Griffiths, M. E. Inall, and W. R. Turrell (2008), Quantifying the overflow across the Wyville Thomson Ridge into the Rockall Trough, *Deep Sea Res., Part I*, *55*, 396–404.
- Smagorinsky, J. (1963), General circulation experiments with the primitive equations, I. The basic experiment, *Mon. Weather Rev.*, *91*, 99–164.
- Smith, W. H. F., and D. T. Sandwell (1997), Global seafloor topography from satellite altimetry and ship depth soundings, *Science*, *277*, 1957–1962.
- Stansfield, K., C. Garrett, and R. Dewey (2001), The probability distribution of the Thorpe displacement within overturns in Juan de Fuca Strait, *J. Phys. Oceanogr.*, *31*, 3421–3434.
- Thorpe, S. A. (1977), Turbulence and mixing in a Scottish loch, *Philos. Trans. R. Soc. London, Ser. A*, *286*, 125–181.
- Timmermans, M. L., C. Garrett, and E. Carmack (2003), The thermohaline structure and evolution of the deep waters in the Canadian Basin, Arctic Ocean, *Deep Sea Res., Part I*, *50*, 1305–1321.
- Toole, J. M., K. L. Polzin, and R. W. Schmitt (1994), Estimates of diapycnal mixing in the abyssal ocean, *Science*, *264*, 1120–1123.
- Toole, J. M., R. W. Schmitt, K. L. Polzin, and E. Kunze (1997), Near-boundary mixing above the flanks of a midlatitude seamount, *J. Geophys. Res.*, *102*, 947–959.
- Turrell, W. R., G. Slessor, R. D. Adams, R. Payne, and P. A. Gillibrand (1999), Decadal variability in the composition of Faroe Shetland Channel bottom water, *Deep Sea Res., Part I*, *46*, 1–25.
- Wunsch, C. (1998), The work done by the wind on oceanic general circulation, *J. Phys. Oceanogr.*, *28*, 2332–2340.
- Zilberman, N. V., J. M. Becker, M. A. Merrifield, and G. S. Carter (2009), Model estimates of M_2 internal tide generation over Mid-Atlantic Ridge topography, *J. Phys. Oceanogr.*, *39*, 2635–2651.

R. A. Hall, Department of Oceanography, University of Hawai'i at Mānoa, Marine Science Building, 1000 Pope Rd., Honolulu, HI 96822, USA. (rhall@soest.hawaii.edu)

J. M. Huthnance, National Oceanography Centre, Joseph Proudman Building, 6 Brownlow St., Liverpool L3 5DA, UK.

R. G. Williams, Department of Earth and Ocean Sciences, University of Liverpool, 4 Brownlow St., Liverpool L69 3GP, UK.